



Cite this: *Chem. Commun.*, 2020, 56, 14283

Received 13th August 2020,  
Accepted 23rd October 2020

DOI: 10.1039/d0cc05513a

rsc.li/chemcomm

## All-nanoparticle layer-by-layer coatings for Mid-IR on-chip gas sensing†

Diana Al Hussein<sup>a</sup>, Junchao Zhou<sup>b</sup>, Daniel Willhelm<sup>a</sup>, Trevor Hastings<sup>a</sup>, Gregory S. Day<sup>c</sup>, Hong-Cai Zhou<sup>a,c</sup>, Gerard L. Coté<sup>d</sup>, Xiaofeng Qian<sup>a</sup>, Ricardo Gutierrez-Osuna<sup>e</sup>, Pao Tai Lin<sup>a,b</sup> and Svetlana A. Sukhishvili<sup>a,\*</sup>

**Functionalization of optical waveguides with submicron coatings of zinc peroxide (ZnO<sub>2</sub>) and silica (SiO<sub>2</sub>) nanoparticles (NPs) is reported that enabled selective concentration of acetone vapors in the vicinity of the waveguide, boosting the sensitivity of a mid infrared (MIR) on-chip detector. Controlled thickness was achieved by introducing precise control of the substrate withdrawal speed to the layer-by-layer (LbL) deposition technique.**

Mid infrared (MIR) gas sensors are potentially advantageous over solid-state sensors, such as metal-oxide (MOX) and conducting polymer (CP) chemiresistors. Mainly, MOX and CP type of sensors have broad cross-selectivity, which hinders their ability to detect and quantify gases in mixtures or complex environments.<sup>1–3</sup> In contrast, MIR gas sensors can be extremely selective due to their ability to measure specific IR vibrational absorption peaks of the target analyte(s). However, such sensors require long optical path lengths for enhanced absorption.<sup>4,5</sup> To address this fundamental issue, a novel and simple functionalization method is proposed that provides precise control of substrate withdrawal speed during layer-by-layer (LbL) deposition.

The LbL technique has become an invaluable tool for constructing thin conformal polymer and nanocomposite coatings using sequential deposition from aqueous solutions.<sup>6–8</sup> Interestingly, the entire field of LbL film assembly was inspired by an early report by Iler on developing coatings from aqueous solutions of oppositely charged millimicron-size colloidal particles.<sup>9</sup>

However, it is challenging to construct LbL coatings from aqueous solutions composed of solely inorganic NPs, which have high curvature, small particle–particle contact area, and high tendency to aggregation. Aside from Iler, successful all-NP LbL film assembly has only been reported by one research group.<sup>10–12</sup> These prior studies demonstrate control of film porosity and refractive index *via* varying NP arrangements through different assembly pH to achieve desired antireflection, antifogging, and self-cleaning performance. However, because of the use of a conventional LbL deposition technique, the resulting films were patchy and unstable at early deposition stages, reaching uniform morphology with full substrate coverage only after tens of deposition cycles.

To address these issues, precise control of the substrate withdrawal speed during LbL assembly was used to achieve ultrathin robust coatings at the very first steps of NP deposition. The goal was to maximize the number of NPs within the evanescent wave distance from the substrate (typically few hundreds of nanometers)<sup>13</sup> to enable MIR detection of analyte molecules selectively adsorbed on NPs surfaces. The controlled substrate withdrawal technique is inspired by early work by Landua and Levich on the formation of continuous monolayer films from sol–gel colloidal solutions<sup>14–19</sup> and more recently from polymeric solutions.<sup>20–23</sup> To our knowledge, this study is the first report on all-nanoparticle film assembly from aqueous solutions using the LbL technique in combination with control of substrate withdrawal speed. The hybrid technique reported here enabled the deposition of homogeneous films, which achieved full coverage after only a few bilayers (BLs). Finally, we applied these submicron coatings to MIR waveguides, rendering them sensitive and selective to the detection of acetone vapors.

The films were assembled from aqueous solutions of positively charged zinc peroxide (ZnO<sub>2</sub>) and negatively charged silica (SiO<sub>2</sub>) NPs and characterized as described in detail in the ESI.† ZnO<sub>2</sub> NPs were synthesized *via* oxidative hydrolysis of a zinc salt as reported previously,<sup>24,25</sup> while spherical SiO<sub>2</sub> NPs were purchased from Sigma Aldrich. X-ray diffraction (XRD)

<sup>a</sup> Department of Materials Science and Engineering, Texas A&M University, College Station, TX 77843, USA. E-mail: svetlana@tamu.edu

<sup>b</sup> Department of Electrical and Computer Engineering, Texas A&M University, College Station, TX 77843, USA

<sup>c</sup> Department of Chemistry, Texas A&M University, College Station, TX 77843, USA

<sup>d</sup> Department of Biomedical Engineering, Texas A&M University, College Station, TX 77843, USA

<sup>e</sup> Department of Computer Science and Engineering, Texas A&M University, College Station, TX 77843, USA

† Electronic supplementary information (ESI) available: Experimental and characterization details along with supplementary figures. See DOI: 10.1039/d0cc05513a

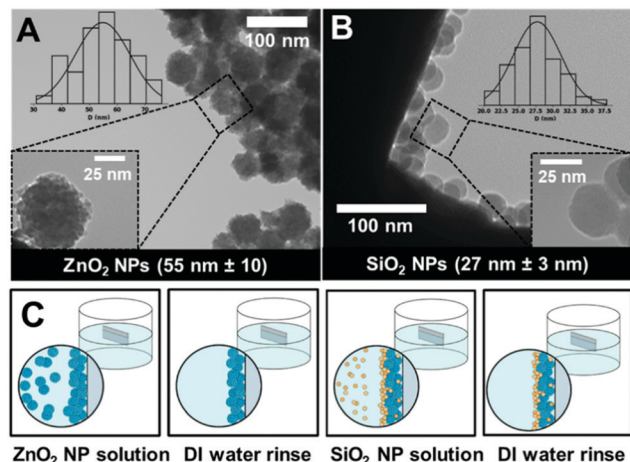


**Fig. 1** Transmission scanning microscopy (TEM) images for ZnO<sub>2</sub> (A) and SiO<sub>2</sub> (B) NPs. The histograms were generated by analyzing 200 particles in several TEM images using imageJ software. Schematic illustrating LbL dipping technique (C).

characterization suggested cubic (Pa3) crystal structure for ZnO<sub>2</sub> NPs and amorphous structure for SiO<sub>2</sub> NPs (Fig. S1A and B, respectively, ESI†). Transmission electron microscopy (TEM) analysis indicated size distribution of diameter of 55 nm ± 10 nm for the ZnO<sub>2</sub> nanoclusters and 27 nm ± 3 nm for the SiO<sub>2</sub> NPs (Fig. 1A and B). Raspberry-like ZnO<sub>2</sub> nanoclusters consisted of ZnO<sub>2</sub> NPs of approximately 4 nm in diameter. ZnO<sub>2</sub> and SiO<sub>2</sub> aqueous solutions were prepared at concentrations of 0.2 wt% at pH 5.5 and 10, respectively. These solution conditions gave rise to zeta potentials of +34.1 ± 8.5 mV for ZnO<sub>2</sub> NPs (isoelectric point (IEP) = 8)<sup>26</sup> and −37.4 ± 4.5 mV for SiO<sub>2</sub> NPs (IEP = 1.8).<sup>27</sup> Dynamic light scattering (DLS) analysis showed good dispersity of these NPs in the aqueous solutions used for LbL assembly, where ZnO<sub>2</sub> and SiO<sub>2</sub> NPs hydrodynamic diameters were 111.4 nm (PDI = 0.21) and 26.9 nm (PDI = 0.17), respectively (Fig. S2A and B, ESI†). Using our modified LbL deposition technique with substrate withdrawal speed control, we show the capability to develop films of varied substrate coverages and thicknesses. The optimized films of uniform coverage and desired thickness were utilized to functionalize optical waveguides to enable acetone vapor detection.

ZnO<sub>2</sub>/SiO<sub>2</sub> films were first deposited on silicon (Si) substrates (see ESI† for the cleaning procedure). In both conventional and precisely controlled depositions, the precleaned Si substrates were first immersed in 0.2% aqueous solution of ZnO<sub>2</sub> NPs at pH 5.5, followed by thorough rinsing in deionized (DI) water. Then, the substrate was immersed in 0.2% aqueous solution of SiO<sub>2</sub> NPs at pH 10 followed by thorough rinsing. This four-step dipping process constituted one BL deposition (Fig. 1C) and was repeated multiple times. Two deposition techniques were used here; conventional and precisely controlled. For conventional LbL deposition, manual dipping with fast/uncontrolled withdrawal of substrates from the deposition solutions was used. In the case of precisely controlled deposition, a dipping robot (DR-3 Table Top Dipping Device, Riegler & Kirstein GmbH) was used, and the substrate was withdrawn

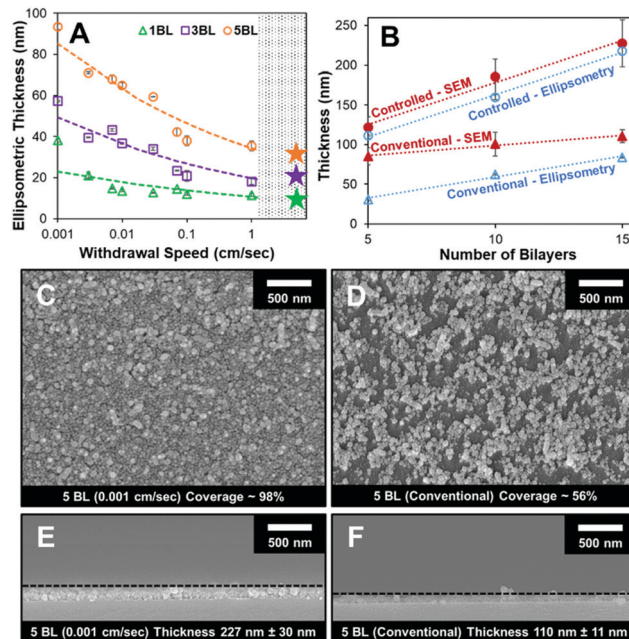


**Fig. 2** Ellipsometric thickness of ZnO<sub>2</sub>/SiO<sub>2</sub> BL films in logarithmic scale for precisely controlled dipping as a function of substrate withdrawal speeds and conventional dipping (represented by star symbol) for 1-, 3- and 5-BL films (A); comparison of ellipsometric and cross-sectional SEM thicknesses as a function of number of bilayers for precisely controlled and conventional dipping (B); top-view and cross-sectional SEM images of 5-BL films deposited using precisely controlled dipping at 0.001 cm s<sup>−1</sup> substrate withdrawal speed (C) (E) and using conventional dipping (D), (F). Thicknesses were evaluated using Image J software (refer to Fig. S6, ESI† for further details).

from the NP aqueous solutions at different speeds. In both cases, substrate withdrawal was preceded by 5 minute static equilibration in the dipping solution. The chosen speeds ranged between 0.001 and 1 cm s<sup>−1</sup> representing both the convective capillary regime and the Landua-Levich advective draining regime (Fig. S3, ESI†).<sup>17</sup> At lower substrate withdrawal speeds, often < 0.01 cm s<sup>−1</sup>, the film assembly is governed by the evaporation rate of the liquid. However, at higher substrate withdrawal speeds, often > 0.1 cm s<sup>−1</sup>, the film assembly is mainly controlled by density, viscous drag and surface tension of the liquid.<sup>14,15,17,28</sup> Fig. 2A shows that ellipsometric thicknesses of 1-, 3- and 5-BL films decreased with increasing substrate withdrawal speed. The dependence of the film thickness on substrate withdrawal speed has been previously explored in other experimental systems, *i.e.* continuous single-step deposition of monolayer of polymers or colloidal particles where the “V”-shape dependence was found.<sup>19–23</sup> In these prior publications, the film thickness decreased with withdrawal speed in the capillary regime because of the shorter time allowed for the particles to entrain the liquid at the meniscus. However, at higher substrate withdrawal speeds, a slight increase in film thickness was observed due to the onset of advection, *i.e.* an enhanced diffusion of the deposited material in a solvent caused by an increased motion of the substrate. At the intersection of these two regimes, the

contributions of both capillary and advective effects were the weakest resulting in thinner films.<sup>17,19</sup>

In the case of our all-NP film assembly, no minimum in the film thickness was observed, and the overall film thickness continued to decrease with the substrate withdrawal speed. The lack of an increase in film thickness at higher withdrawal speeds characteristic for the draining regime is due to the weak effect of the advective forces on the assembly of rigid, high-curvature/small-size nanoparticles whose assembly is dominated by the capillary forces.

Whereas ellipsometric results in Fig. 2A reveal the overall area-averaged density of NPs deposited on the substrate, SEM studies give local information on the homogeneity of the film. Fig. 2B shows that, while both techniques indicate a linear increase in film thickness with the number of bilayers, the controlled deposition technique yielded thicker films (1.5 to 2.5-fold thicker films at the dipping speed  $0.001 \text{ cm s}^{-1}$ ). The ellipsometry and SEM results were in good agreement for automatically deposited films, and significantly differed for the conventional LbL coatings. These results reflect the different packing density of NPs in these films. Specifically, for conventional LbL films, SEM measurements of the overall height of the films have ignored voids and inhomogeneities within the films, while spectroscopic ellipsometry did account for those by measuring a low refractive index of 1.2 for 5-, 10- and 15-BL films. In contrast, the difference between the film thicknesses determined by the two techniques was minimal in the case of more homogeneous, denser coatings (refractive index of 1.33 for 5-BL films and 1.4 for 10- and 15-BL films) deposited using the controlled substrate deposition technique, reflecting denser NP packing. The difference in film quality prepared by the two techniques is further evident in Fig. 2C and D. It is seen that, for the same number of film deposition cycles (5-BL films), precisely controlled dipping with extremely slow substrate withdrawal speed enabled uniform films with 98% substrate coverage, while conventional dipping resulted in non-uniform patchy films with only 56% substrate coverage. The non-uniform deposition of film during conventional dipping is also obvious from the cross-sectional SEM images (Fig. 2E and F). Note that, for the controlled NP film deposition with withdrawal speeds  $< 0.01 \text{ cm s}^{-1}$ , a stripe pattern was observed in the films at low BL numbers ( $< 5$  BLs), and this pattern disappeared when withdrawal speed was greater than  $0.01 \text{ cm s}^{-1}$  (Fig. S4 and S5A–J, ESI†). This pattern is due to a “stick-slip” phenomenon, which is determined by the degree of wettability of the substrate and evaporation rate of the dipping solution.<sup>19,29–31</sup> In contrast to earlier work on monolayer deposition of NPs, where similar patterns were observed, in our case the deposition of the next layer of NPs is not only controlled by capillary forces at extremely low withdrawal speeds, but also by electrostatic attraction to previously deposited NPs. Importantly, as the number of layers exceeded 5 BLs, the stripe patterns were no longer observed as deposition of additional layers smoothen the overall film morphology. Atomic force microscopy (AFM) images further confirm that the controlled substrate withdrawal yields more uniform film morphology (Fig. S7, ESI†).

The ability of these all-NP thin films to adsorb acetone molecules was then studied. First-principles density functional

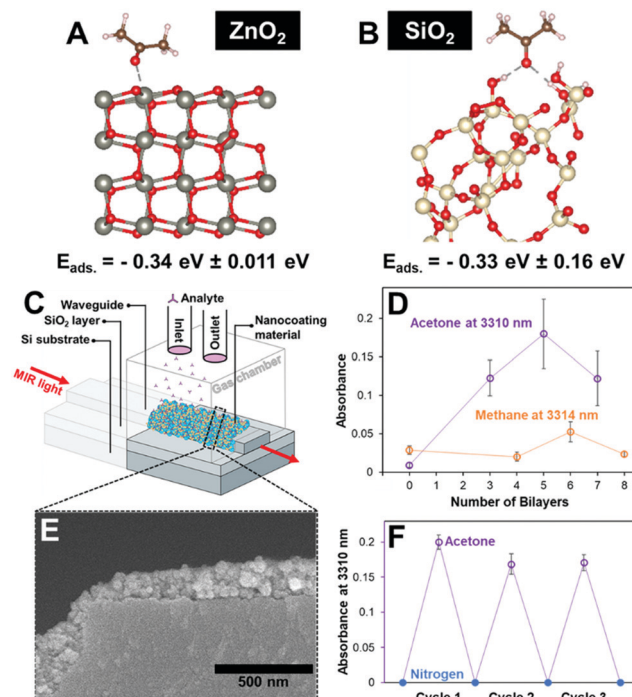


Fig. 3 The preferential adsorption configuration of acetone molecule on the surface of  $\text{ZnO}_2$  and amorphous  $\text{SiO}_2$  nanoparticle (A) and (B); schematic representation of waveguide-based sensor (C); cross sectional SEM image of functionalized waveguide with 5 BLs (E). Graphs showing absorbance of acetone and methane as a function of number of bilayers at 3310 nm and 3314 nm, respectively (D) and acetone reversibility of the measurements (F).

theory (DFT)<sup>32,33</sup> calculations were performed to estimate adsorption energy ( $E_{\text{ads}}$ ) of acetone molecules on the surface of  $\text{ZnO}_2$  and amorphous  $\text{SiO}_2$  NPs. Computational details of surface adsorption energies can be found in the (ESI†). Fig. 3A and B show the preferential adsorption among various potential adsorption configurations of the acetone carbonyl group on the (100)  $\text{ZnO}_2$  surfaces and on the silanol groups of  $\text{SiO}_2$ . The averaged adsorption energies are  $0.35 \pm 0.011$  and  $0.33 \pm 0.16 \text{ eV}$  per acetone molecule for  $\text{ZnO}_2$  and a- $\text{SiO}_2$ , respectively, indicating a relatively strong physisorption. Hence, both  $\text{ZnO}_2$  and amorphous  $\text{SiO}_2$  NPs can strongly adsorb acetone molecules on their surface, enhancing their concentration in the vicinity of waveguide for on-chip MIR sensing.

Finally, the ability of the NP coatings to enhance sensitivity and selectivity of the on-chip MIR sensing of acetone was examined experimentally (Fig. 3C). The a-Si waveguides were prepared by complementary metal-oxide-semiconductor (CMOS) processes capable of fabrication of wafer-scale MIR sensing platforms (see the ESI† for waveguide fabrication and gas measurement setup details). Fig. 3E shows that the precisely controlled dipping technique at  $0.001 \text{ cm s}^{-1}$  enabled deposition of uniform NP coatings on the waveguides. In order to detect acetone vapor, a characteristic band at 3310 nm corresponding to a mixed C–H stretching vibration was used.<sup>34</sup> Fig. 3D shows that acetone could not be detected by bare waveguides, because of the overall low number of molecules within the vicinity of the



evanescent field (penetration depth of 200 nm). Note that bare waveguide is represented as 0-BL coating in Fig. 3D. In contrast, deposition of ZnO<sub>2</sub>/SiO<sub>2</sub> NP coatings enabled acetone detection at its characteristic vibrational frequency. The absorbance calculated using Beer's law increased from  $0.0091 \pm 0.0029$  for the bare waveguide (0 BLs) to  $0.18 \pm 0.045$  for 5-BL coating, yielding more than a 10-fold increase in sensitivity. In order to confirm the selectivity nature of these coatings, the absorbance of a non-polar gas (methane) was measured at one of its characteristic bands, 3314 nm. Absorbance increased from  $0.029 \pm 0.0054$  for the bare waveguide to maximum of  $0.052 \pm 0.013$  for 6-BL coating, indicating preferential selectivity and sensitivity of the coating to polar vapors such as acetone. Next, reversibility of acetone vapors was examined to ensure the ability to use the prototype sensor multiple times. Fig. 3F shows that adsorption of acetone within the coating is reversible, and adsorbed molecules can be removed from the coating in 30 seconds *via* nitrogen gas purge. The nature of the acetone adsorption on the nanoparticles was confirmed *via* vapor sorption analysis on a Micromeritics ASAP 2420. The ZnO<sub>2</sub> NPs show reversible adsorption of acetone vapor, with only minimal hysteresis, representing the presence of strong physisorption. For comparison, acetone adsorption on the SiO<sub>2</sub> NPs was also performed, which did not show any appreciable hysteresis and showed overall lower adsorption affinity, despite its higher surface area – as determined by the Brunauer–Emmett–Teller (BET) method<sup>35</sup> (see ESI† for N<sub>2</sub> and vapor sorption isotherms as well as details on the surface area analysis *via* the BET method, Fig. S12 and S13, ESI†). Hence, our computational and experimental results are in good agreement.

In conclusion, the potential of this novel and hybrid technique was shown including the use of conventional LbL deposition with controlled substrate withdrawal speed in depositing uniform all-nanoparticle conformal coatings. The coating of micro-fabricated on-chip waveguide substrates enabled enhanced sensitivity of MIR detection of acetone vapors at an analyte-characteristic wavelength. The developed technique of NP coating deposition has the potential to be used for spectroscopic detection of analytes relevant in optical, biomedical, and environmental applications.

Financial support for this research was from the Texas A&M President's Excellence Fund X-Grant (G. L. C.; R. G.-O.; P. T. L.; S. S.), the National Science Foundation (NSF) under grant no. OAC-1835690 (X. Q.); and the Robert A. Welch Foundation for a Welch Endowed Chair (H.-C. Z, A-0030). The Materials Characterization Facility (MCF), Microscopy Imaging Center (MIC), Soft Matter Facility (SoMF) and Department of Chemistry at Texas A&M University are acknowledged for use of their characterization instrumentation and staff contributions. Qing Zhou and Angelo Kirchon are acknowledged for their help in collecting AFM and isotherm data, respectively.

## Conflicts of interest

There are no conflicts to declare.

## Notes and references

- 1 A. D. Wilson, *Metabolites*, 2015, **5**, 140–163.
- 2 H. T. Nagle, R. Gutierrez-Osuna and S. S. Schiffman, *IEEE Spectrum*, 1998, **35**, 22–34.
- 3 R. Gutierrez-Osuna, *IEEE Sens. J.*, 2002, **2**, 189–202.
- 4 T. N. Jin, J. C. Zhou, H. Y. G. Lin and P. T. Lin, *Anal. Chem.*, 2019, **91**, 817–822.
- 5 T. N. Jin, J. C. Zhou and P. T. Lin, *RSC Adv.*, 2020, **10**, 7452–7459.
- 6 A. Zhuk and S. A. Sukhishvili, *Soft Matter*, 2013, **9**, 5149–5154.
- 7 V. Selin, J. F. Ankner and S. A. Sukhishvili, *Macromolecules*, 2017, **50**, 6192–6201.
- 8 X. Zhang, Y. Xu, X. Zhang, H. Wu, J. Shen, R. Chen, Y. Xiong, J. Li and S. Guo, *Prog. Polym. Sci.*, 2019, **89**, 76–107.
- 9 R. K. Iler, *J. Colloid Interface Sci.*, 1966, **21**, 569–594.
- 10 D. Lee, M. F. Rubner and R. E. Cohen, *Nano Lett.*, 2006, **6**, 2305–2312.
- 11 J. P. DeRocher, P. Mao, J. Y. Kim, J. Han, M. F. Rubner and R. E. Cohen, *ACS Appl. Mater. Interfaces*, 2012, **4**, 391–396.
- 12 D. Lee, D. Omolade, R. E. Cohen and M. F. Rubner, *Chem. Mater.*, 2007, **19**, 1427–1433.
- 13 T. Jin, H.-Y. G. Lin and P. T. Lin, *ACS Appl. Mater. Interfaces*, 2017, **9**, 42905–42911.
- 14 L. Landau and B. Levich, *Acta Physicochim. URSS*, 1942, **17**, 42–54.
- 15 J. A. Britten, *Chem. Eng. Commun.*, 1993, **120**, 59–71.
- 16 N. Krins, M. Faustini, B. Louis and D. Grosso, *Chem. Mater.*, 2010, **22**, 6218–6220.
- 17 T. Schneller, R. Waser, M. Kosec and D. Payne, *Chemical solution deposition of functional oxide thin films*, 2016, ch. 10, pp. 233–261.
- 18 M. Faustini, B. Louis, P. A. Albouy, M. Kuemmel and D. Grosso, *J. Phys. Chem. C*, 2010, **114**, 7637–7645.
- 19 J. Gao, S. Semlali, J. Hunel, D. Montero, Y. Battie, D. Gonzalez-Rodriguez, R. Oda, G. L. Drisko and E. Pouget, *Chem. Mater.*, 2020, **32**, 821–829.
- 20 S. Roland, R. E. Prud'homme and C. G. Bazuin, *ACS Macro Lett.*, 2012, **1**, 973–976.
- 21 S. Roland, D. Gaspard, R. E. Prud'homme and C. G. Bazuin, *Macromolecules*, 2012, **45**, 5463–5476.
- 22 A. Vital, M. Vayer, T. Tillocher, R. Dussart, M. Boufnichel and C. Sinturel, *Appl. Surf. Sci.*, 2017, **393**, 127–133.
- 23 M. Vayer, A. Pineau, F. Warmont, M. Roulet and C. Sinturel, *Eur. Polym. J.*, 2018, **101**, 332–340.
- 24 M. Sun, W. C. Hao, C. Z. Wang and T. M. Wang, *Chem. Phys. Lett.*, 2007, **443**, 342–346.
- 25 D. Sebok, L. Janovak and I. Dekany, *Appl. Surf. Sci.*, 2010, **256**, 5349–5354.
- 26 C. Bergs, P. Simon, Y. Prots and A. Pich, *RSC Adv.*, 2016, **6**, 84777–84786.
- 27 G. A. Parks, *Chem. Rev.*, 1965, **65**, 177–198.
- 28 M. Faustini, C. Boissiere, L. Nicole and D. Grosso, *Chem. Mater.*, 2014, **26**, 709–723.
- 29 J. X. Huang, R. Fan, S. Connor and P. D. Yang, *Angew. Chem., Int. Ed.*, 2007, **46**, 2414–2417.
- 30 J. X. Huang, F. Kim, A. R. Tao, S. Connor and P. D. Yang, *Nat. Mater.*, 2005, **4**, 896–900.
- 31 S. Watanabe, K. Inukai, S. Mizuta and M. T. Miyahara, *Langmuir*, 2009, **25**, 7287–7295.
- 32 P. Hohenberg and W. Kohn, *Phys. Rev.*, 1964, **136**, B864–B871.
- 33 W. Kohn and L. J. Sham, *Phys. Rev.*, 1965, **140**, A1133–A1138.
- 34 G. Dellepiane and J. Overend, *Spectrochim. Acta*, 1966, **22**, 593–614.
- 35 S. Brunauer, P. H. Emmett and E. Teller, *J. Am. Chem. Soc.*, 1938, **60**, 309–319.